Laparoscopic near-infrared hyperspectral imaging system for identifying living porcine nerves and unexposed arteries

TOSHIHIRO TAKAMATSU,^{1,*} D SEIYA HAYASHI,² NARIAKI OKAMOTO,³ SHINTARO ARAKAKI,^{3,4} ABIÁN GUEDES HERNÁNDEZ,⁵ NOBUYOSHI TAKESHITA,⁶ HIRO HASEGAWA,³ HIDEO YOKOTA,⁷ KOHEI SOGA,⁸ GUSTAVO MARRERO CALLICO,⁵ D AND HIROSHI TAKEMURA²

Abstract: Surgical resection remains a key curative option for cancer, with minimally invasive approaches increasingly adopted. To enhance intraoperative visualization, we developed a laparoscopic near-infrared hyperspectral imaging (NIR-HSI) system comprising a custom laparoscope, supercontinuum light source, and acousto-optic tunable filter. Ex vivo NIR-HSI of porcine arteries, mesentery, and nerves revealed distinct spectral signatures from 1000–1402 nm. Pixel-based classification via neural networks achieved >99% accuracy, sensitivity, and specificity in most cases. In vivo imaging of a living pig enabled identification of exposed nerves (88.4% accuracy, 68.7% recall) and unexposed arteries (83.2% accuracy, 60.2% recall). These results demonstrate that laparoscopic NIR-HSI can differentiate tissues with similar coloration and detect structures embedded beneath the surface, offering potential for safer minimally invasive surgeries.

© 2025 Optica Publishing Group under the terms of the Optica Open Access Publishing Agreement

1. Introduction

As the number of surgical procedures increases, along with the incidence of more complex cases, there is a growing need for the development of surgical support systems that can recognize anatomical structures, such as adjacent organs, blood vessels, and nerves, that should be preserved [1–3]. Such systems are essential for performing minimally invasive surgery more safely and easily, reducing postoperative complications, and improving patient quality of life.

Recently, computer-assisted surgery (CAS) has become a key technology for supporting surgical operations [4]. Computer-assisted surgery includes a variety of technologies that can enhance the diagnosis, treatment, and overall clinical management of healthcare. Moreover, CAS has become popular in abdominal surgery, where it is frequently used to aid in different surgical procedures. Kitaguchi et al. and Kojima et al. constructed a model that automatically recognized the root of the inferior mesenteric artery and nerve in real time during laparoscopic

#576004 Journal © 2025

¹ Health and Medical Research Institute, National Institute of Advanced Industrial Science and Technology, Tsukuba, Ibaraki, Japan

²Department of Mechanical and Aerospace Engineering, Faculty of Science and Technology, Tokyo University of Science, Noda, Chiba, Japan

³Department of Colorectal Surgery, National Cancer Center Hospital East, Chiba, Japan

⁴Graduate School of Medicine, University of the Ryukyus, Okinawa, Japan

⁵Institute for Applied Microelectronics (IUMA), University of Las Palmas de Gran Canaria, Las Palmas de Gran Canaria, Spain

⁶Department of the Promotion of Medical Device Innovation, National Cancer Center Hospital East, Chiba, Japan

⁷RIKEN Center for Advanced Photonics, Wako, Saitama, Japan

⁸Department of Materials Science and Technology, Faculty of Advanced Engineering, Tokyo University of Science, Tokyo University of Science, Katsushika-ku, Tokyo, Japan

*takamatsu-t@aist.go.jp

colorectal surgery using a deep learning-based semantic segmentation approach [5,6]. However, relying on visible wavelength information allows only the recognition of surface-exposed areas, and distinguishing tissues with similar colors and shapes can be challenging. Therefore, to achieve or exceed the level of area prediction based on the experience of specialists, training machine-learning models with information beyond visible light imaging is necessary.

Currently, several imaging techniques have been proposed for visualizing specific biological tissues, such as blood flow assessment using indocyanine green (ICG) and nerve visualization with fluorescent probes [7–9]. In addition, other modalities with potential applications include optoacoustic imaging [10], laser-induced breakdown spectroscopy (LIBS) [11,12], and optical coherence tomography (OCT) [13]. ICG imaging has been approved for clinical use; however, in blood flow evaluation, its fluorescence decays about 30 minutes, which limits its continuous application [14]. Regarding nerve visualization with fluorescent probes, no clinically approved agents are currently available. Furthermore, for optoacoustic imaging, LIBS, and OCT, no systems have been reported that can perform simultaneous imaging during laparoscopic surgery, and significant challenges remain for their application in computer-assisted surgery. Therefore, the development of new imaging modalities is required.

Near-infrared (NIR) light ranges from approximately 700 to 2500 nm, which is longer than that of visible light. Compared with visible and ultraviolet light, which have even shorter wavelengths, near-infrared light exhibits two notable characteristics. First, NIR light has high biological tissue penetration due to its low absorption and scattering by water in tissues [15]. Second, the wavelength bands of the molecular overtone vibrations vary depending on the type of molecule, which enables the analyses of the components of biological tissues via observations of the spectra in the infrared region [16]. Therefore, these two features may be used in laparoscopic surgery to identify tissues that exist deep in the body and those that are difficult to distinguish from visible tissues.

Sato et al. and Mitsui et al. identified regions of gastrointestinal stromal tumors and gastric cancer located deep in the normal mucosa (approximately 2 mm thickness) using 1000 to 1600 nm NIR-hyperspectral imaging (NIR-HSI) [17,18]. These reports suggest that deep tissues other than lesions can also be visualized. Additionally, we developed laparoscopic systems capable of NIR-HSI above 1000 nm [19,20]. Therefore, by performing NIR-HSI during laparoscopic surgery, identifying crucial tissues, such as nerves and arteries located deep within tissues that are difficult to distinguish with visible light is expected. In this study, NIR-HSI was performed in an in vivo porcine open surgery model to evaluate the feasibility of NIR-HSI laparoscopy for clinical surgery.

2. Materials and methods

2.1. Laparoscopic NIR-HSI system

As shown Fig. 1, a laparoscopic NIR-HSI system was developed. The imaging optics of the laparoscopic NIR-HSI system were designed as follows. The system uses a custom-made laparoscope (3MX-1760, Machida Endoscope Co., Tokyo, Japan) that transmits visible to near-infrared light and an image with a 40° field of view (FOV). The image was split by a short-pass dichroic mirror with a 950 nm threshold (DMSP950, Thorlabs, USA) and focused by various lenses (LA5012, AC254-150-AB, AC254-100-AB, AC254-075-C Thorlabs, USA) onto a visible camera and near-infrared camera. The visible monochrome camera was a complementary metal oxide semiconductor (CMOS) camera (CS130-B, SHODENSYA Co., Ltd., Osaka, Japan) that was sensitive to wavelengths of 450–950 nm, and the near-infrared camera was an InGaAs camera (ARTCAM-990SWIRTEC, ARTRAY Co., Ltd., Tokyo, Japan) sensitive to wavelengths of 450-1700nm. To mitigate chromatic aberration effects when imaging across a wide wavelength range, a liquid lens with an electrically adjustable focal length (EL-16-40-NIR-5D-C; Optotune,

Dietikon, Switzerland) was placed behind the laparoscope. The image can be resolved up to 2–4.5 lp/mm at 1000–1400 nm wavelengths [20].

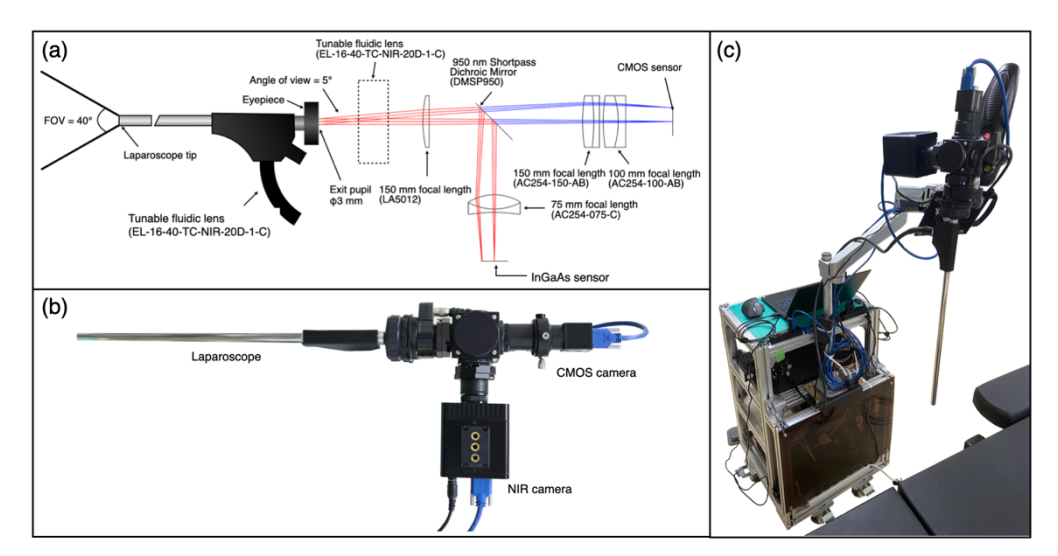


Fig. 1. (a) Diagram of an optical system of the laparoscope using visible and NIR light. (b) Imaging part of the laparoscope. (c) Overall view of the developed NIR-HSI laparoscopic system.

To acquire the NIR-HSI data, we employed a staring method to extract and image each wavelength of the light source [21]. We used a high-intensity supercontinuum (SC) light source (SC-OEM, Wuhan Yangtze Soton Laser Co., Ltd., Wuhan, China) and an acoustic optical tunable filter (AOTF-PRO, Wuhan Yangtze Soton Laser Co., Ltd., Wuhan, China) to extract various wavelengths [20]. Light spectrally separated by the AOTF is output as highly coherent light, which is subsequently diffused to approximately 33° using a top hat-type diffuser (EDC-30) and input into a 6 mm diameter bundle-type light guide illuminated from the tip of the laparoscope [20]. For the camera settings, the gain was set to the maximum value for each camera, and a 99% reflectance standard (SG3052, SphereOptics GmbH, Germany) was placed 60 mm from the tip of the laparoscope to obtain white data. The exposure time for each wavelength was set to ensure that the maximum pixel value was less than 90% of the dynamic range within 2000ms.

2.2. NIR-HSI for ex vivo porcine tissue

To investigate whether the developed device can acquire NIR-HSI and enable identification through machine learning, NIR-HSI from 1000–1402 nm at 6 nm intervals was performed at a measurement distance of 60 mm on the arterial tissue, mesentery, and nerve tissue extracted from a slaughtered pig. The resulting HSI contain 67 bands. The reason for using this wavelength range is that absorption originating from molecular vibration is known to appear at 1000 nm and above [22]. However, in previous deep lesion classifications using excised specimens, absorption originating from water appeared strongly at wavelengths above 1400 nm [17] and signal-to-noise ratio was low to utilize as data for tissue classification. Therefore, we decided to acquire data at wavelengths of up to 1400 nm, and NIR-HSI data were obtained for each type of tissue resected from two different locations. As NIR pseudocolor images, RGB assignment was based on two wavelengths with relatively high reflectance (1036 and 1282 nm) and one with strong absorption (1372 nm), arranged in ascending order [17].

2.3. NIR-HSI for an in vivo pig

Because ex vivo specimens lack blood flow, the spectra obtained in vivo are expected to differ. Therefore, as shown in Fig. 2(a), we anesthetized an LDW pig (female, $40 \, \mathrm{kg}$; KAC Co., Ltd.). The imaging targets were the exposed obturator nerves in the lower abdomen and the artery (aorta) hidden deep within other tissues, as shown in Fig. 2(b) and (c), respectively. The image acquisition setup was the same as for the ex vivo experiment. In addition, pseudovisible color images were captured at three wavelengths (R = $700 \, \mathrm{nm}$, G = $604 \, \mathrm{nm}$, and B = $556 \, \mathrm{nm}$) using the AOTF output to create annotated data. Because the light output was insufficient below $556 \, \mathrm{nm}$, longer wavelengths were assigned to the RGB channels to approximate visible images. Ventilation was stopped during imaging to prevent organ movement. The two different nerve sites were imaged at four different angles. Four different vessel sites were imaged at two different angles. In this study, ventilation was stopped during imaging because the subject moved with ventilation.

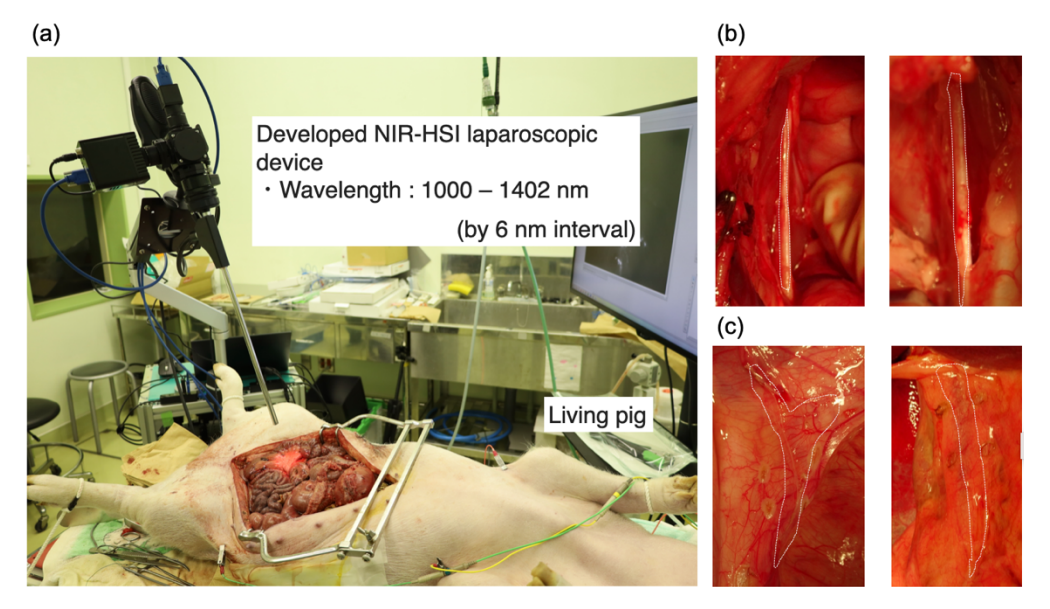


Fig. 2. (a) NIR-HSI setup under in vivo evaluation. Visible image of captured (b) nerve and (c) artery tissue.

All the procedures and protocols were approved by the Animal Care and Use Committee of the National Cancer Center (K21-020).

2.4. Data processing

Calibrating each pixel is necessary to analyze the images. Here, (i, j) denotes dark noise and white standard images. Additionally, to convert each reflectance to absorbance, the calibration was performed as follows:

$$A(i,j) = -log_{10} \left(\frac{I_r(i,j) - I_d(i,j)}{I_w(i,j) - I_d(i,j)} \right),\,$$

where A(i,j) is the row vector of the absorbance spectrum of the obtained image and $I_r(i,j)$, $I_w(i,j)$, and $I_d(i,j)$ are the row vectors of the raw data, white standard data, and dark data, respectively. When $I_w(i,j) - I_d(i,j)$ was less than zero, the pixel was excluded from the calculation.

To correct the magnification and location changes caused by chromatic aberration correction using a variable-focus liquid lens, AKAZE local features and affine transformations were

performed on the images obtained at each wavelength for image registration [23]. For noise

performed on the images obtained at each wavelength for image registration [23]. For noise reduction, the affine transformed spectra were smoothed using the Savitzky–Golay method with a window size of 2N + 1 for 11 points, and the order of the approximation equation was set to 3 [24].

2.5. Model algorithm

Subsequently, an annotation mask was created to obtain the target spectrum from the NIR-HSI data. For the in vivo NIR-HSI data, the locations of the nerves and arteries were annotated by a surgeon on each NIR-HSI image. Because these arteries are located deep, they are difficult to identify in visible images. Therefore, a mask was created by confirming the positions of the exposed blood vessels after imaging. To mask the border between the targets and other tissues, 16 pixels of the boundary were excluded. In addition, the surgical instruments and fingers of the surgeon were excluded from the masks.

Spectra obtained from each pixel within the annotation mask were used to identify tissues by applying machine learning on a per-pixel basis. The learning method employed a three-layer neural network [25]. In this study, the leave-one-out cross-validation method was employed. When creating a learning model for a specific site, data from that site were excluded from the training set to avoid overfitting, and only data from other sites were used. Because machine learning classification outputs a probability of 0 to 1, we set the threshold value at 0.6 to examine whether the targets could be specifically classified [19].

The prediction accuracy was evaluated by classifying the pixels into four groups: target predicted as target (true positive: TP), target predicted as other tissues (false negative: FN), other tissues predicted as target (false positive: FP), and other tissues predicted as other tissues (true negative: TN). From the classified pixels, the specificity, recall, and accuracy were calculated as follows:

$$Specificity \ [\%] = \frac{TN}{FP + TN} \times 100;$$

$$Recall \ [\%] = \frac{TP}{TP + FN} \times 100;$$

$$Accuracy \ [\%] = \frac{TP + TN}{TP + TNFPFN} \times 100.$$

3. Results

In this system, light could separate the visible and near-infrared wavelengths, and the images were captured using visible and near-infrared cameras. In the investigation using resected porcine organs, NIR-HSI data from 1000–1402 nm were obtained for each subject at 6 nm intervals. The average spectrum of each tissue was extracted, as shown in Fig. 3(a).

The shape of the spectrum differed among the three tissue types: arterial, fat, and nerve. The dataset was created using each pixel as training data, and when the pixel was classified into three classes by the neural network, it could be visualized as shown in Figs. 3(b, i–vi). The accuracy, sensitivity, and specificity exceeded 99%, except for the specificity for the nerve, as shown in Table 1.

Table 1. Prediction results from the NIR-HSI analysis for ex vivo tissue

	Accuracy (%)	Recall (%)	Specificity (%)	
Artery	99.3	99.4	99.3	
Fat	99.2	99.1	99.8	
Nerve	99 4	99.4	86.5	

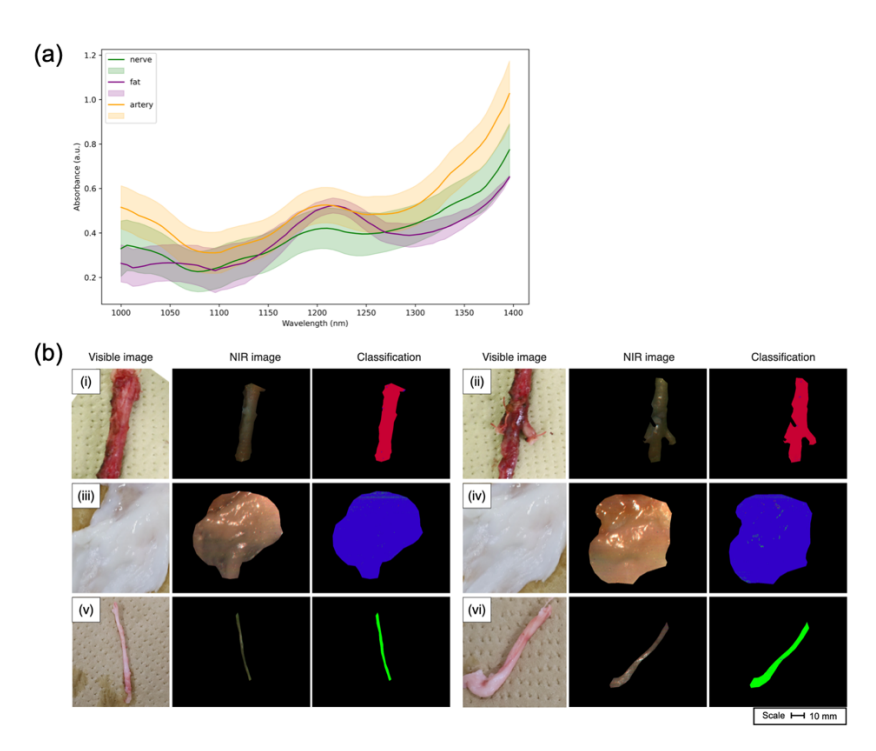


Fig. 3. (a) NIR spectrum of each tissue. The colored areas represent the standard deviation of each spectrum. (b) Neural network classification of ex-vivo pig tissues. Panels (i) and (ii) show arteries, panels (iii) and (iv) show fat, and panels (v) and (vi) show nerves. The left image in each panel is a visible image. The center image in each panel is an NIR pseudocolor image using 1036 nm for red, 1282 nm for green, and 1372 nm for blue. The right image in each panel is an image classified by a neural network. Each red, blue, and green pixel indicates a classification of artery, fat, and nerve, respectively.

In the living pig imaging, NIR-HSI can be performed with an imaging time of approximately 25 s. Although a slight blur between wavelengths was observed owing to the suspension of ventilation during imaging, these images could be corrected via affine transformation. Based on the annotated image pixels, the spectral data of the exposed and unexposed nerves were acquired as shown in Figs. 4(a) and (b), respectively. A significant difference in absorption exists over a wide range of the near-infrared region for nerves, arteries, and other tissues.

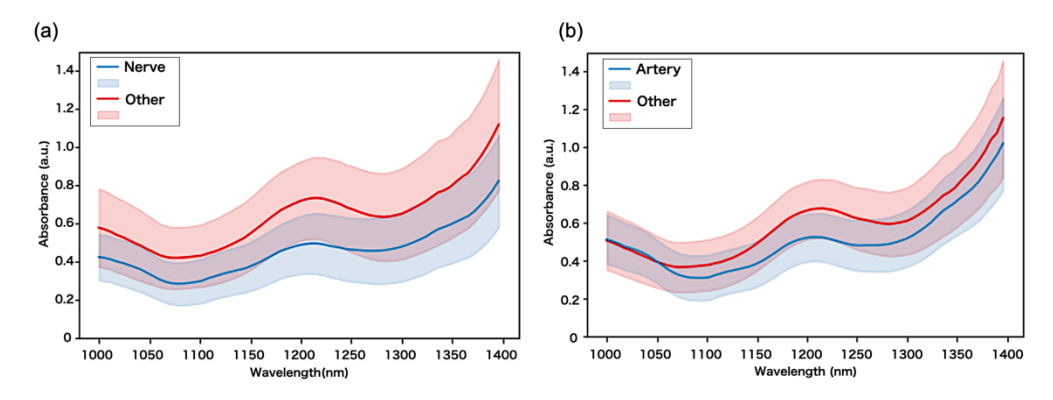


Fig. 4. Acquired NIR spectra of (a) exposed nerves and (b) non-exposed blood vessels.

Figure 5 shows images of the exposed nerves (two locations) captured and classified using the NIR-HSI laparoscopic system from four different angles. Each pixel was classified into two classes based on the nerve and other tissues, and the exposed nerves were detected as TPs across all the scenes. However, there were also confirmed situations in which there were more FPs, depending on the angle. The overall accuracy, recall, and specificity of the exposed nerves were 88.4%, 68.7%, and 89.1%, respectively (Table 2).

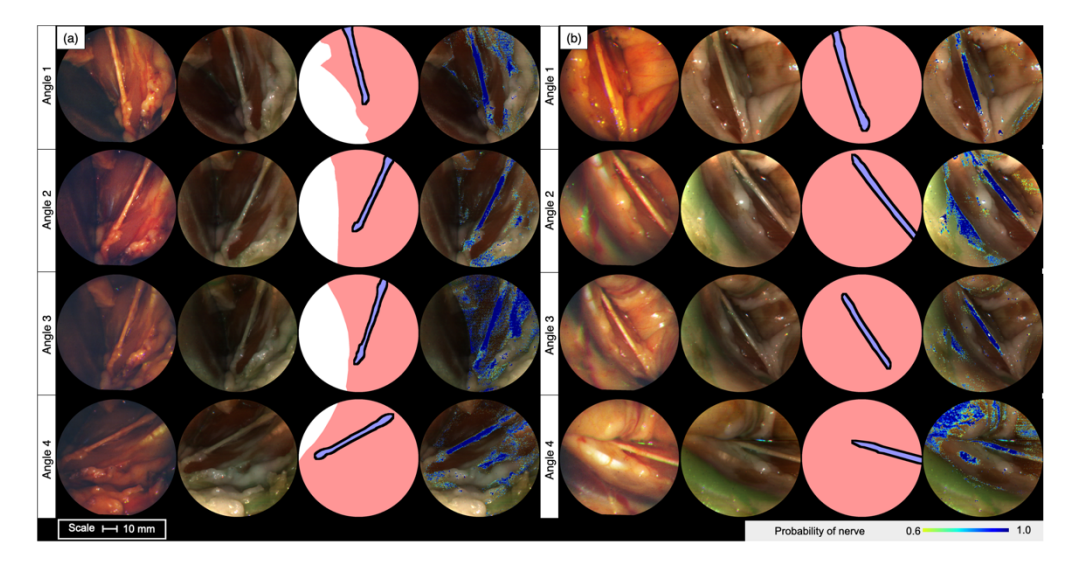


Fig. 5. Four-angle images of in vivo exposed nerves in two locations of the lower abdomen (a and b). From left to right: visible pseudocolor image (R: 700 nm, G: 604 nm, and B: 556 nm), near-infrared pseudocolor image (R: 1036 nm, G: 1282 nm, B: 1372 nm), annotation image, and overlay image in the visible image with classified pixels. In the annotation images, the blue areas represent pixels of the nerve regions, and the red areas represent other tissue pixels. The black areas at the boundaries between blue and red are margin pixels that were excluded from the training to prevent incorrect annotations. White areas representing retractor was annotated as pixels to be excluded from training, similar to the margin pixels. The classification images display probabilities from 0.6 to 1.0 in a heatmap.

Table 2. Classification results of the NIR-HSI analysis for exposed nerves

Target		Testing pixel (pix)		A a ayyma ayy (61.)	Dagol1 (01)	Considerity (01)
Nerve	Angle	Nerve	Other tissues	Accuracy (%)	Recall (%)	Specificity (%)
(a)	1	16014	346056	87.2	81.8	87.4
	2	14268	386582	91.9	75.7	92.5
	3	14060	346343	72.7	76.7	72.5
	4	13973	506752	90.1	74.0	90.6
(b)	1	25943	528955	96.4	59.6	98.2
	2	21533	531187	88.8	61.5	90.0
	3	13395	542414	96.1	67.0	96.8
	4	15319	550407	84.3	53.5	85.1
Average		-	-	88.4	68.7	89.1

Figure 6 shows images of the unexposed vessels (four locations) captured and classified using the NIR-HSI laparoscopic system from two angles. The surface capillaries and peritoneum are

transparent, and the arteries hidden deep in the tissue, which are difficult to recognize in visible images, are observable in near-infrared images. Machine learning classification confirmed that deep arteries could be detected in the imaged scenes. The overall accuracy, recall, and specificity for non-exposed arteries were 83.2%, 60.2%, and 88.0%, respectively (Table 3).

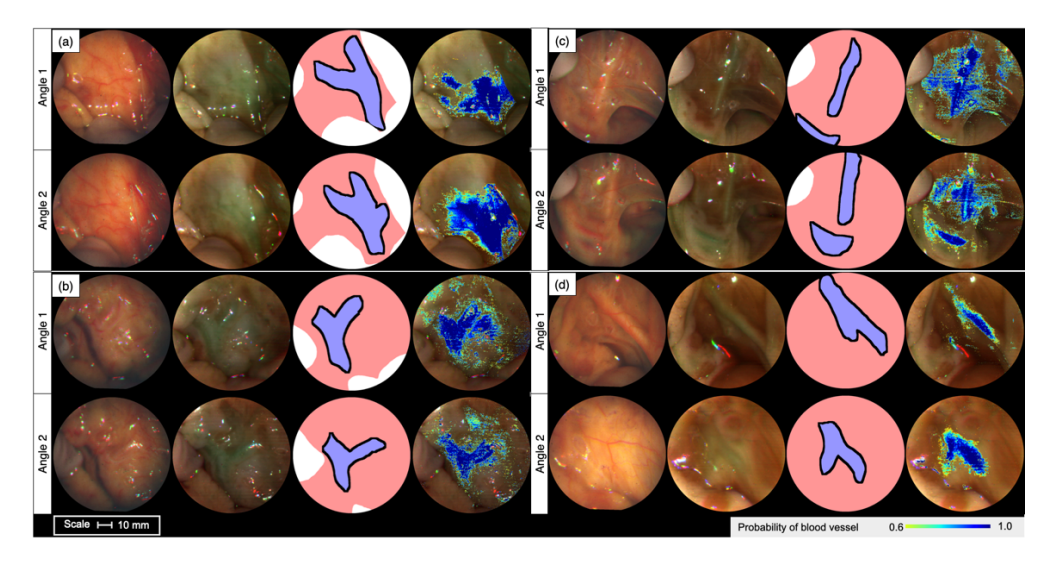


Fig. 6. Two-angle images of unexposed arteries (aorta) in four locations (a–d). From left to right: visible pseudocolor image (R: 700 nm, G: 604 nm, and B: 556 nm), near-infrared pseudocolor image (R: 1036 nm, G: 1282 nm, B: 1372 nm), annotation image, and overlay image in the visible image with classified pixels. The annotation image and classification image are color-coded in the same manner as are those in Fig. 5. In the annotation images, white areas representing human fingers were annotated as pixels to be excluded from training.

Target Testing number of pixels (pix) Accuracy (%) Recall (%) Specificity (%) Blood Vessel Angle Artery Other tissues 110869 229528 70.6 45.6 82.7 (a) 2 104555 284953 80.6 80.2 80.8 1 77763 402579 85.5 82.5 67.1 (b) 2 57468 435899 89.4 75.4 91.2 1 462282 75.9 54.6 79.0 68464 (c) 2 80757 436214 82.0 55.8 86.9 85257 89.0 465220 32.6 99.4 (d) 2 60557 494572 95.3 70.5 98.4 83.2 60.2 88.0 Average

Table 3. Classification results of NIR-HSI analysis for unexposed arteries

4. Discussion

In this study, the NIR-HSI system developed for laparoscopy was used for ex vivo and in vivo imaging of porcine tissues. In the ex vivo study, when the NIR-HSI data were acquired for each tissue, differences in shape were observed in the average near-infrared spectrum of each tissue, and the neural network could classify each tissue into multiple classes with high accuracy.

In an in vivo investigation, the NIR spectra and visible-wavelength images of living pig nerves and unexposed arteries were obtained under a laparoscope. This demonstrates that NIR-HSI can be acquired simultaneously with conventional laparoscopic imaging, indicating its feasibility for application in laparoscopic surgery. Although we used only one pig for this study, because the NIR spectral information was acquired and analyzed for each pixel, the amount of training data for classification was considered sufficient for an exploratory study. Unlike conventional image classification approaches, our method treats each pixel as an individual training sample, thereby enabling the acquisition of a large volume of training data that is proportional to the number of pixels. By training a neural network on the acquired spectral information, we demonstrated that the device can display the locations of the targets as images. However, to ensure generalized classification performance, it is necessary to acquire more training data from multiple pigs in future studies.

As shown in Fig. 4(a), comparing the average spectra of the nerves and other tissues revealed differences in absorption across wavelengths, especially in the shape near 1200 nm, which may have contributed to the classification. As shown in Fig. 4(b), comparing the average spectra of the deep arterial region and other regions revealed that the absorption spectra crossed at approximately 1060 nm and that the difference was maximal at approximately 1200 nm, which is considered to have contributed to the classification. However, when the same area was imaged from multiple angles and the classification results were analyzed using machine learning, the accuracy varied significantly when the angle was changed. These results are thought to be attributable to the changes in halation and scattering caused by changes in the angle of lighting. Although many FP pixels were observed in the classification of nerves, some areas that were TN were identified in the classification results of other angles. Thus, TP can possibly be identified via movie-based classification. Although recall was generally low, the classification of unexposed arteries showed a particularly low average recall of 60.2%. In this study, the probability threshold was set at 0.6, which contributed to the decrease in recall. In addition, the low recall rate may be due to the varying depths of the arteries, with the sensitivity of the deeper targets being lower. Although it is difficult to identify depth sensitivity in in vivo studies, previous NIR-HSI studies using excised specimens have reported the visualization of unexposed cancer, which is covered with approximately 3 mm-thick normal tissue [18]. Thus, this study also intended to visualize tissues more than 3 mm deep under laparoscopy. However, the observable depth differs among tissue types. For example, the peritoneum tends to be more translucent, whereas fat tissue is comparatively opaque. Hence, further validation is necessary.

To realize movie-based classification, it is necessary to accelerate the imaging and identification processes. In this study, the imaging and classification processes required approximately 25 s and several minutes, respectively. A reduction in the time required for these processes is considered achievable in the future through the following improvements: (i) selection of wavelengths that are effective for classification, (ii) development of light sources that are capable of rapidly switching between effective wavelengths, and (iii) correction of chromatic aberrations.

(i) The number of wavelengths can be significantly reduced by selecting key wavelengths that distinguish different tissues. Akimoto et al. and Yahata et al. reported that NIR-MSI using four wavelengths selected from to 1000–1600 nm can be used for the regional classification of unexposed gastrointestinal stromal tumors and gastric cancer without a significant loss of accuracy from NIR-HSI analysis results [26,27]. Therefore, it is possible to avoid scanning all wavelengths if the wavelengths necessary for discrimination are selected. (ii) Hayashi et al. reported a near-infrared LED light source for an NIR-MSI rigid endoscopy system that can capture images at 9 wavelengths in 0.5 s and performs classification via machine learning in 1.5 s [28]. Because the development of light sources using LEDs allows for the customization of output wavelengths and potential increases in intensity, faster image acquisition is expected in the future [29]. In addition, achieving rapid identification using NIR-HSI data is difficult

because the calculation cost of employing an algorithm that learns the shape of an image, such as a convolutional neural network, is prohibitive [30,31]. However, if the number of wavelengths is reduced, then the calculation cost can be significantly reduced, and further improvements in accuracy can be expected [14]. (iii) The time required for device control, particularly the adjustment of the focal length with a liquid-tunable lens, is a critical factor. In the current system, focal-length adjustment is necessary because of the optical system within the laparoscope, and it takes 100 ms to switch the wavelength. Therefore, correction of the chromatic aberration of the laparoscopic lens should be customized. Our group has already developed a prototype relay lens for laparoscopes that considers the near-infrared region above 1000 nm. Moreover, and wide-area chromatic aberration correction has been confirmed (patent application in Japan: No. 2025-069098). Therefore, we believe that a laparoscope with chromatic aberration correction in the visible and near-infrared regions can be developed in the future.

By satisfying each of the above issues, NIR-HSI under laparoscopic surgery is expected to be a technique for CAS, not only for the classification of similarly colored tissues but also for the visualization of objects that are buried deep in the tissue and should not be damaged (e.g., nerves, arteries, prostate, ureters, and bile ducts).

5. Conclusion

In this study, we developed an NIR-HSI laparoscope system integrated with conventional visible imaging and demonstrated its application to machine learning analysis of biological tissues in both ex vivo and in vivo experiments. Our results suggest that NIR-HSI has the potential to differentiate tissues with similar surface coloration and to identify structures embedded beneath the surface, thereby reducing the risk of injuring critical tissues during laparoscopic surgery. However, the current system still requires optimization in terms of acquisition speed, robustness in vivo, and clinical usability. Future studies will focus on refining the hardware and algorithms, as well as conducting animal and observational studies to validate its potential for safer minimally invasive surgery.

Funding. Japanese Society for the Promotion of Science KAKENHI (21H038440, 24K03315, 25K03501); AMED (23ym0126806j0002, 24he0422027j0002, A417TS); Futaba Foundation (243023).

Acknowledgment. We express our sincere gratitude to Mr. Ryodai Fukushima (Department of Mechanical and Aerospace Engineering, Faculty of Science and Technology, Tokyo University of Science) for his valuable assistance with the data analysis.

Disclosures. The authors have no relevant financial or other potential conflicts of interest to disclose.

Data availability. Data presented in this study are available upon request from the corresponding author.

References

- H. Sung, J. Ferlay, R. L. Siegel, et al., "Global cancer statistics 2020: GLOBOCAN estimates of incidence and mortality worldwide for 36 cancers in 185 countries," Ca-Cancer J. Clin. 71(3), 209–249 (2021).
- D. Moszkowicz, B. Alsaid, T. Bessede, et al., "Where does pelvic nerve injury occur during rectal surgery for cancer?" Colorectal Disease 13(12), 1326–1334 (2011).
- D. Kitaguchi, N. Takeshita, H. Matsuzaki, et al., "Computer-assisted real-time automatic prostate segmentation during TaTME: a single-center feasibility study," Surgical Endoscopy 35(6), 2493–2499 (2021).
- H. G. Kenngott, M. Wagner, F. Nickel, et al., "Computer-assisted abdominal surgery: new technologies," Langenbecks Arch. Surg. 400(3), 273–281 (2015).
- D. Kitaguchi, N. Takeshita, H. Matsuzaki, et al., "Real-time vascular anatomical image navigation for laparoscopic surgery: experimental study," Surgical Endoscopy 36(8), 6105–6112 (2022).
- S. Kojima, D. Kitaguchi, T. Igaki, et al., "Deep-learning-based semantic segmentation of autonomic nerves from laparoscopic images of colorectal surgery: an experimental pilot study," International Journal of Surgery 109(4), 813–820 (2023).
- S.-C. Chen, M.-C. Wang, W.-H. Wang, et al., "Fluorescence-assisted visualization of facial nerve during mastoidectomy: A novel technique for preventing iatrogenic facial paralysis," Auris Nasus Larynx 42(2), 113–118 (2015).
- E. M. Walsh, D. Cole, K. E. Tipirneni, et al., "Fluorescence Imaging of Nerves During Surgery," Ann. Surg. 270(1), 69–76 (2019).

- Y.-J. Lee, R. K. Orosco, M. Bouvet, et al., "Intraoperative nerve-specific fluorescence visualization in head and neck surgery: a Phase 1 trial," Nat. Commun. 16(1), 6060 (2025).
- D. Jüstel, H. Irl, F. Hinterwimmer, et al., "Spotlight on Nerves: Portable Multispectral Optoacoustic Imaging of Peripheral Nerve Vascularization and Morphology," Adv. Sci. 10(19), 2301322 (2023).
- H. Abbasi, L. M. Beltrán Bernal, A. Hamidi, et al., "Combined Nd:YAG and Er:YAG lasers for real-time closed-loop tissue-specific laser osteotomy," Biomed. Opt. Express 11(4), 1790–1807 (2020).
- H. Abbasi, R. Guzman, P. C. Cattin, et al., "All-fiber-optic LIBS system for tissue differentiation: A prospect for endoscopic smart laser osteotomy," Optics and Lasers in Engineering 148, 106765 (2022).
- 13. A. E. Carolus, M. Lenz, M. Hofmann, *et al.*, "High-resolution in vivo imaging of peripheral nerves using optical coherence tomography: a feasibility study," Journal of Neurosurgery **132**(6), 1907–1913 (2020).
- L. Ayala, T. J. Adler, S. Seidlitz, et al., "Spectral imaging enables contrast agent–free real-time ischemia monitoring in laparoscopic surgery," Sci. Adv. 9(10), eadd6778 (2023).
- 15. A. M. Smith, M. C. Mancini, and S. Nie, "Second window for in vivo imaging," Nat. Nanotechnol. 4(11), 710–711 (2009).
- B. M. Nicolaï, K. Beullens, E. Bobelyn, et al., "Nondestructive measurement of fruit and vegetable quality by means of NIR spectroscopy: A review," Postharvest Biol. Technol. 46(2), 99–118 (2007).
- D. Sato, T. Takamatsu, M. Umezawa, et al., "Distinction of surgically resected gastrointestinal stromal tumor by near-infrared hyperspectral imaging," Sci. Rep. 10(1), 21852 (2020).
- T. Mitsui, A. Mori, T. Takamatsu, et al., "Evaluating the identification of the extent of gastric cancer by over-1000 nm near-infrared hyperspectral imaging using surgical specimens," J. Biomed. Opt. 28(08), 086001 (2023).
- T. Takamatsu, Y. Kitagawa, K. Akimoto, et al., "Over 1000 nm Near-Infrared Multispectral Imaging System for Laparoscopic In Vivo Imaging," Sensors 21(8), 2649 (2021).
- T. Takamatsu, R. Fukushima, K. Sato, et al., "Development of a visible to 1600 nm hyperspectral imaging rigid-scope system using supercontinuum light and an acousto-optic tunable filter," Opt. Express 32(9), 16090 (2024).
- 21. Q. Li, X. He, Y. Wang, *et al.*, "Review of spectral imaging technology in biomedical engineering: achievements and challenges," J. Biomed. Opt. **18**(10), 1–29 (2013).
- C. Pasquini, "Near Infrared Spectroscopy: fundamentals, practical aspects and analytical applications," J. Braz. Chem. Soc. 14(2), 198–219 (2003).
- 23. I. Eichhardt and D. Barath, "Optimal Multi-view Correction of Local Affine Frames," arXiv (2019).
- M. Člupek, P. Matějka, and K. Volka, "Noise reduction in Raman spectra: Finite impulse response filtration versus Savitzky–Golay smoothing," J. Raman Spectrosc. 38(9), 1174–1179 (2007).
- 25. T. Udelhoven and B. Schütt, "Capability of feed-forward neural networks for a chemical evaluation of sediments with diffuse reflectance spectroscopy," Chemom. Intell. Lab. Syst. **51**(1), 9–22 (2000).
- K. Akimoto, R. Ike, K. Maeda, et al., "Wavelength Bands Reduction Method in Near-Infrared Hyperspectral Image based on Deep Neural Network for Tumor Lesion Classification," European Journal of Applied Sciences 9(1), 273–281 (2021).
- 27. A. Yahata, H. Takemura, R. Iwanami, *et al.*, "Gastric Cancer Detection by Two-step Learning in Near-Infrared Hyperspectral Imaging," Journal of Information and Communication Engineering **7**(2), 467–473 (2021).
- S. Hayashi, T. Takamatsu, N. Kakuta, et al., "Near-Infrared Multispectral Imaging Rigid Endoscope System for High-Speed Target Identification Using LED Rotating Light Source," Advanced Biomedical Engineering 14(0), 79–88 (2025).
- M. Naeeme, S. Maysam, D. James, et al., "LED-based, real-time, hyperspectral imaging device," J. Med. Imag. 12(03), 035002 (2025).
- N. Okamoto, M. R. Rodríguez-Luna, V. Bencteux, et al., "Computer-Assisted Differentiation between Colon-Mesocolon and Retroperitoneum Using Hyperspectral Imaging (HSI) Technology," Diagnostics 12(9), 2225 (2022).
- 31. E. Bannone, T. Collins, A. Esposito, *et al.*, "Surgical optomics: hyperspectral imaging and deep learning towards precision intraoperative automatic tissue recognition—results from the EX-MACHYNA trial," Surgical Endoscopy **38**(7), 3758–3772 (2024).